Fifth International Symposium on Marine Propulsors
smp'17, Espoo, Finland, June 2017

Simulation-driven Design of a Rim Drive for an Autonomous Vehicle

Heinrich Grümmer[1], Stefan Harries[2] and Andrés Cura Hochbaum[3]

[1]aXatlantic, Potsdam, Germany
[2]FRIENDSHIP SYSTEMS AG, Potsdam, Germany
[3]Technical University of Berlin, Berlin, Germany

ABSTRACT

A hub-less, Rim-Driven Thruster (RDT) was designed and optimized for maximum attainable speed of an Autonomous Surface Vehicle (ASV) targeted to cross the Atlantic. Viscous flow simulations in open-water condition were performed using OpenFOAM. The CFD setup was validated with experimental data from (Oosterveld 1970). The accuracy in performance prediction was enhanced by incorporating empirical models accounting for the friction within nozzle and rim. Parametric models for the nozzle and propeller blades allow the variation of geometry with very few defining parameters. The definition of the nozzle's section was based on class-and-shape transformation (CST) methodology and allowed the investigation of a wide range of shape variants.

While both, the simulation-ready CAD and optimizations were realized within CAESES, fully automatic grid generation was achieved by integrating Pointwise into the process. A resistance test was conducted at TU Berlin's towing tank for the unappended hull to allow the estimation of the vessels speed for different thruster variants. The optimization was based on a surrogate model and performed for five free variables. Starting from a baseline design an overall improvement of speed from 1.22 m/s to 1.46 m/s was achieved.

Keywords Rim-Driven Thruster, Simulation-Driven Design (SDD), Autonomous Surface Vehicle, Computer Aided Engineering (CAE), Computational Fluid Dynamics.

1 INTRODUCTION

In (Grümmer et al 2017), detailed insight into the concept and engineering of the solar-powered aXatlantic ASV is provided. A semi-perforated hull design stemming from a comprehensive hydrostatic optimization process, allows a self-righting and time-dependent stability behavior of the vessel that carefully matches the requirements of an ASV designated to cross the Atlantic.

For further advancement of the system, a hub-less RDT was chosen as a means of propulsion. As opposed to a conventional propeller, driven via its shaft, the torque driving the blades of an RDT is delivered via a surrounding ring that is structurally connected to the blade tips. By implementing it as a steerable thruster unit, the risk of entanglement of the unmanned ASV is reduced and maneuverability is improved. The absence of a hub allows for objects to pass through the unit without interference. A high flow velocity area in the center of the shaft-less thruster supports the free passage of any debris that otherwise might lead to fouling of the propeller (Freeman & Marshall 2011). The absence of a hub and shaft also diminishes the frictional losses and eliminates dissipation due to formation of a hub vortex (Cao et al 2011). As the blade tips are connected directly to the rim, no tip leakage vortex exists. The compact design also helps in saving space, allows for a flexible mounting and aids in the reduction of secondary systems (Cao et al 2011, Hughes et al 2000 & Yakovlev et al 2011). Furthermore, the nozzle creates directional stability and provides exceptional maneuverability due to thrust vectoring of the steerable unit, as well as protection for the propeller blades.

As the main operating condition of the vessel concentrates on higher advance ratios and light screw loading, the nozzle section needs to be chosen with respect to low viscous and pressure drag (Oosterveld 1970). Flow separation, as observed on heavily loaded nozzles, is not an issue but too light loading also leads to an increasing drag, as a large surface area induces unnecessary high skin-friction. Consequently, the nozzle's length to diameter ratio must be kept as small as possible. This puts high requirements on the electric motor embedded in the nozzle. Only a low radial height allows for a profile of low drag and as the rim will be connected directly to the rotor, the axial length should not exceed the rim's dimension. As (Oosterveld 1970) states, the major disadvantage of RDTs over conventional ducted propellers is that the ring, surrounding the propeller, needs to be countersunk into the nozzle. This creates a small gap which is filled with fluid and the evolving flow leads to tangible frictional losses. The CFD simulations in this work do not include this gap and the neglect of friction is accounted for by empirical models, subsequently.

Based on the amount and efficiency of the solar-cells, as well as the intended geographic position range and operating season, an approximated minimum continuously available power for the propulsion was estimated. Within this work, optimized performance of the vessel has been targeted. Based on an SDD process, the cruising speed was maximized utilizing the given amount of energy.

2 REFERENCE SIMULATION

To verify the correctness of the results obtained from CFD simulations during the optimization, an initial reference

simulation was set up. To allow for comparison with existing experimental findings a combination of a Ka4-70 propeller in nozzle 19A was examined.Oosterveld (1970) provides open-water diagrams for this exact combination at various ratios of pitch to diameter P/D out of which $P/D = 0.8$ was replicated.

2.1 OpenFOAM Simulation Setup

As the propeller is four-bladed, simulating only a $1/4$ segment of the computational domain helped saving CPU time. Rotational symmetric matching grids were handled by a `cyclic` boundary condition, and `cyclicAMI` was applied in cases of non matching surface meshes.

The domain was furthermore split up into a rotating propeller-region and a stationary domain-region. The interfaces between those separate grids were again linked through OpenFOAM's arbitrary mesh interface (AMI) handling capability. However, a more sophisticated way of interpolating between those surfaces sliding along each other was needed. As the overlap changes with each time step, `cyclicPeriodicAMI` boundary condition was applied to achieve correct interpolation. A fully structured hexahedral grid was used and a wall function approach along with the k-ω SST turbulence model was applied to reduce cell count.

2.2 Verification

To assure the reliability of the obtained simulation results, a verification of the CFD setup was performed. Studies on the solution's independence of mesh resolution, size of time step, Reynolds number, number of revolutions simulated and size of computational domain were carried out, subsequently. The resulting total thrust was used as a measure to observe the solution dependence on different factors. The aim was to either find the necessary settings that ensure independence or to quantify the deviation caused by each factor, individually. The settings chosen to be sufficient for upcoming investigations were not solely depending on a specific tolerance but also chosen with respect to the computational costs they induce.

2.2.1 Domain Size and Number of Revolutions

The computational domain is of cylindrical shape and therefore can be specified by a certain inlet- and outlet-length l_i and l_o, measured from the propeller plane, as well as a domain radius R_D. To keep computational costs low and ensure that the domain boundaries do not impact the solution, the three measures l_i, l_o and R_D were altered individually. While changing the expansion in one direction, the other two were kept at the constant reference values $l_i = 6R$, $l_o = 10R$ and $R_D = 7R$. The overall cell count of the mesh at these reference settings was around $1.2e^6$ and changed as the domain size was expanded or reduced during the study.

While l_i and l_o were found to have only minor impact on the solution, the radial extent can be observed to have a large influence as shown in figure 1. The development of recirculating flow affects the solution and is considered to happen more likely at low advance coefficients. Hence, the results shown are obtained from simulations at bollard pull $J = 0$. As nozzle 19A is designed to generate a considerable amount of thrust at low advance ratios this explains the significant impact of R_D on the total thrust.

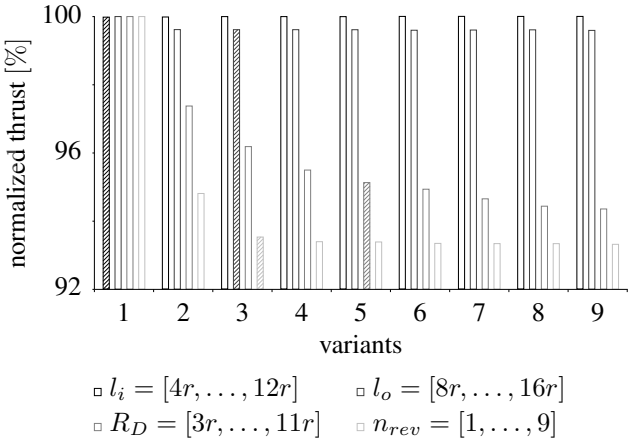

Figure 1: **Dependency of thrust on domain size and number of revolutions. All intervals are split equidistant and bars of values chosen for the optimization are hatched for highlighting.**

To ensure sufficient convergence of forces, the number of revolutions n_{rev} simulated until steady state behavior was reached has been monitored. The change in total thrust over a range of $n_{rev}[1, \ldots, 9]$ shows a sufficient level of convergence after $n_{rev} = 3$ with the difference towards variant 4 being less than 0.14 %.

2.2.2 Reynolds Number and Time Discretization

When setting a specific advance ratio J, the user usually has a free choice on the combination of speed of advance v_a and rotational speed n, as the three measures are related through $v_a = JnD$ with the propeller diameter D. However, each combination results in a different Reynolds number Re.

To gauge the impact of a change in Reynolds number on the solution and allow for a better comparison towards experimental results three different variants where examined. The change in thrust was not rated as an error, but only shows the possible effect that can be observed when examining a certain thruster geometry at different Reynolds numbers. The results given in figure 2 show a distinct dependence of the total thrust on Re. The uncertainty within the investigated interval is however within less than 1 % and not considered problematic with regard to ranking variants.

When setting up simulations at different rotational speeds, the respective time step needs to be adjusted. This allows to keep the number of time steps per revolution and hence, the relative mesh movement per time step at a constant value. The results of three different settings ranging from $n_{steps} = 70$ to 280 steps per revolution are also given in figure 2. Out of the three variants investigated, $n_{steps} = 140$ was chosen for upcoming simulations in order to keep the balance between the solutions accuracy and computational time.

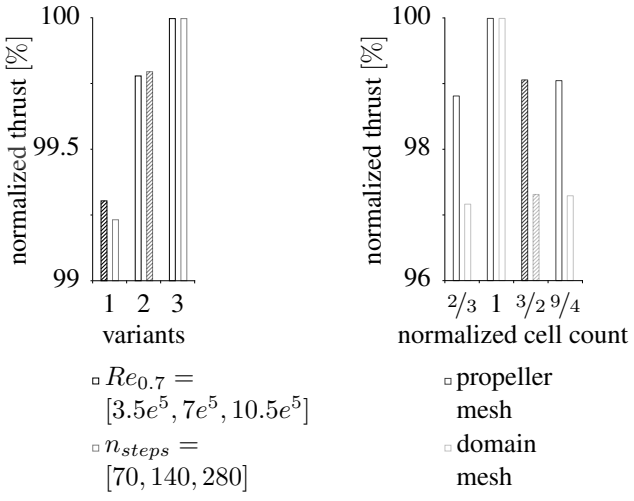

Figure 2: **Effect of Reynolds number and steps per revolution on total thrust (left), as well as impact of changing grid resolution within propeller and domain region (right). Values chosen for the optimization are highlighted.**

2.2.3 Mesh Resolution

The overall cell count for all previous simulations was set at approximately $1e^6$ cells with $2.5e^5$ cells in the propeller region and $7.5e^5$ elements in the domain region. These initial values were chosen, based on similar CFD simulations as in (Subhas 2012 & Bulten 2013). However, a variation of the mesh resolution was necessary to verify a good choice. The number of cells from the coarsest to the finest grid was increased approximately by a factor of $f = 1.5$ with each refinement.

The results already given in figure 2 show a distinct dependency of the calculated thrust on the discretization of the computational domain. Changing the initial resolution of the domain region to the coarse version, lead to a predicted thrust of only 97 %, compared to the solution on the initial mesh. A similar trend was observed, when the initial domain region mesh was kept and the propeller region grid was exchanged for the coarse variant, although the change in thrust was not as significant as in the previous scenario. Increasing the number of cells by a factor of 1.5, in both cases lead to a similar change in thrust and, thus, did not yet allow for any assumptions on the correctness of the solution. After a second refinement the results showed a surprisingly small change. The difference in thrust from $f = 1.5$ to $f = 2.25$ lies at only 0.02 % for the domain mesh and 0.01 % for the propeller mesh. Although this exceptionally good match is likely to be coincidental, it is indicative that the fine mesh at about $1.5e^6$ cells is already adequate for the task at hand.

2.3 Correction of Frictional Dissipation

As the computational model does not account for the friction that occurs inside the gap between the rotating propeller's ring and the nozzle, a certain underestimation of torque was expected. The effect of friction between rim and nozzle was handled by mathematical models separately.

Cao et al. (2015), recently investigated a thruster unit very similar to the one present in this work and divided the gap into the outer, inner and end faces. Based on different empirical formulas the frictional resistance of the three parts was calculated separately. In an earlier publication (2011), Cao et al. applied a similar empirical rim surface correction and validated their results with an experiment.

A number of simulations, varying the axial gap ratio while keeping the radial gap at a constant value and vice versa, were performed and the formulas (1) and (2) were derived. Experiments in a large cavitation tunnel were used for validation and a great improvement in predicting the frictional losses, compared to previous empirical formulas, was found. According to these formulas, the torque of the rim's end and outer surfaces can be calculated as

$$Q_{rim,end} = \left(-0.001634 \cdot \delta^{-1.003} + 0.2282\right) \cdot Re_r^{-0.25} \frac{1}{4} \rho \omega^2 R_o^5 \quad \text{and} \tag{1}$$

$$Q_{rim,out} = 0.01668 \eta^{-1.818} \left(1-\eta\right)^{-1.757} \cdot Re_i^{1.8} 2\pi l_{rim} \rho \nu^2 \quad \text{, with} \tag{2}$$

$$\delta = \frac{s}{R_o} \quad , Re_r = \frac{\omega R_o^2}{\nu} \quad , Re_i = \frac{\omega R_o h}{\nu} \quad \text{and}$$

$$\eta = \frac{R_i}{R_o} \quad .$$

As no exact measurements of the axial and radial gap clearances s and h are given in (Oosterveld 1970), a clearance of $s = 1mm$ in axial and $h = 1mm$ in radial direction was assumed to be reasonable and the additional torque was calculated based on these values. The remaining unknown measures introduced in the equations (1) and (2), are the axial length of the rim which can be obtained from CAD as $l_{rim} = 29.7\ mm$ and the outer radius which is $R_o = R_i + h = 126\ mm$. The rotational speed ω varies with the advance coefficient simulated, the density of the fluid $\rho = 998.21\ {}^{kg}/_{m^3}$ and the kinematic viscosity $\nu = 1.004e^{-6}\ {}^{m^3}/_{s}$ were set to match the properties of freshwater in the tank at $20\ ^\circ C$.

Keeping in mind that the simulated thrust and torque measures are representing only $1/4$ of the thruster, while the additional $Q_{rim,end}$ and $Q_{rim,out}$ apply for the whole unit, the open-water diagram in figure 3 is plotted.

2.4 Comparison

In figure 3, the open-water diagram for the case of ${}^P/_D = 0.8$ reported in (Oosterveld 1970) is shown. The thrust coefficient is split up into two components, namely the nozzle thrust coefficient $K_{T,N}$ and the propeller thrust coefficient $K_{T,P}$ which add up to the total thrust. The simulation results are given in the same diagram.

When looking at the propeller thrust, a very good agreement is found with only a small deviation towards higher thrust values at the advance ratios $J = 0.6$ and $J = 0.7$. A similar trend can be observed when comparing the results of the torque coefficient. In this case, additionally, an underestimation of the torque almost across the whole range of advance coefficients can be seen. The nozzle thrust ap-

pears to be slightly higher then the experimental findings over the whole range of advance ratios. In the case of torque this offset has been anticipated as the consequence of the neglect of friction between the nozzle and rim and was addressed using the empirical models described in the previous section. The corrected values $10K_{Q,cor}$ are also given in the figure 3 and show a much better fit, although the forces are again slightly too high towards higher advance ratios.

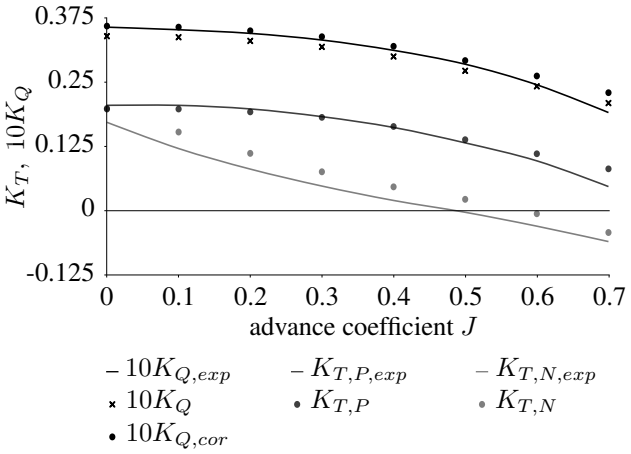

Figure 3: **Open-water diagram from (Oosterveld 1970) and simulation results at $^P/_D = 0.8$.**

3 OPTIMIZATION

A SDD process was followed through in order to identify the most suitable design variant for the application at hand. Based on the verified computational setup described previously, numerous variants were examined and rated.

3.1 Parametric Thruster Design

When it comes to optimization based on variable geometry, a parametric model is needed to provide a simple way of changing the shape by varying its specifying parameters. As a starting point for the exploration algorithm, a baseline design was defined. The nozzle section geometry of this design is based on the CST methodology to allow for maximum variability while keeping the number of design variables within reasonable limits. For the propeller blade a different approach was taken: by starting out with a predetermined design and introducing the design variables by means of re-parametrization of said geometry, a sophisticated propeller can be generated with only a few variables.

3.1.1 Nozzle

As mentioned before, the design of the nozzle is based on the CST methodology. The nozzle itself was created as a surface of revolution of a section which was rotated around the axis of rotation of the propeller. The section is divided into an upper and lower curve, whereby the upper curve represents the part of the nozzle facing away from the propeller towards the surrounding fluid and the lower curve generates the surface facing inwards, towards the axis of rotation. As given in (Lane & Marshall 2009), the two curves can be written in normalized coordinates in lengthwise direction $\psi = {}^x/_c$ and thickness orientation $\zeta = {}^z/_c$ as:

$$\zeta_u(\psi) = C_{N_2}^{N_1}(\psi)\, S_u(\psi) + \psi\Delta\zeta_u \quad \text{and} \tag{3}$$

$$\zeta_l(\psi) = C_{N_2}^{N_1}(\psi)\, S_l(\psi) + \psi\Delta\zeta_l \quad . \tag{4}$$

For a NACA type airfoil with a round nose and pointed end, the exponents of the general class function

$$C_{N_2}^{N_1}(\psi) = \psi N_1 (1-\psi)^{N_2} \tag{5}$$

are set to $N_1 = 0.5$ and $N_2 = 1.0$. The overall shape functions for the upper and lower surfaces are:

$$S_u(\psi) = \sum_{i=0}^{N_u} A_u(i)\, S(\psi, i) \quad \text{and} \tag{6}$$

$$S_l(\psi) = \sum_{i=0}^{N_l} A_l(i)\, S(\psi, i) \quad , \tag{7}$$

with the component shape funktion given as:

$$S(\psi, i) = K_i^n \psi^i (1-\psi)^{N-i} \quad \text{and} \tag{8}$$

$$K_i^n = \frac{n!}{i!\,(n-i)!} \quad . \tag{9}$$

The shape of the upper and lower curves is defined by $N_u = N_l = 3$ parameters out of which only $A_{l,1}$ and $A_{l,2}$ were set as design variables with the others held at constant values of $A_{l,3} = -2$ and $A_{u,i} = 2$, respectively.

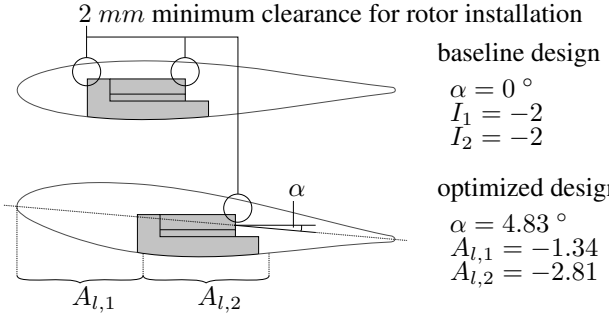

Figure 4: **Parametric nozzle section shape and electric motor (shown schematically in gray) arrangement for baseline and optimized design variant.**

As shown in figure 4, within CAESES, this geometry representation was enhanced by adding a trailing edge radius and the design variable α for the angle of attack. Additionally, the predefined electric motor geometry was taken into account. The section thickness was minimized through scaling of the parameters $A_{k,i}$ for each design based on a minimum clearance and an axially variable motor position.

3.1.2 Propeller

The dimensions of the ASV and consequently the data such as required power input, speed of advance and rotational speed are very small compared to vessels that usually operate in similar environments. It was therefore assumed that criteria such as thrust loading coefficient, strength of

the propeller blades or cavitation number can be neglected. Unsteady forces acting on the hull due to the discrete number of blades were not of any concern either, as they will be of low amplitude and no aspects of comfort need to be considered on an unmanned vessel. The number of propeller blades was consequently set to $n_b = 2$ as the lower surface area aids in reducing viscous forces.

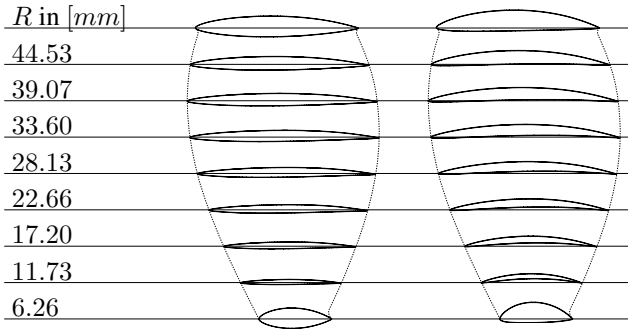

Figure 5: **Expanded blade geometry of baseline (left) and optimized (right) design. A noticeably amount of camber has been introduced during the optimization process.**

To start out with an already reasonably good design and so as to keep the parametric propeller model fairly simple, a baseline design has been generated, based on a set of rough data (see figure 5 on the left). To enable geometry variation of the given blade design, a re-parameterization was performed. The radial distribution of $^P/_D$, as well as the camber as a function of radius were identified. Two design variables $\Delta\alpha$ and Δc were added which allow to change $^P/_D$ as well as the amount of camber.

3.2 Automatic Grid Generation

For an automatic CFD computation of every variant of the changing geometry, an automatic grid generation tool was needed. The basis for each mesh was an IGES export with the geometry data of the design. The process of grid generation was split up into the nozzle and propeller region of the mesh. Using Pointwise, a glyph script was written which handled the grid generation as well as the assignment of boundary conditions and OpenFOAM compatible export.

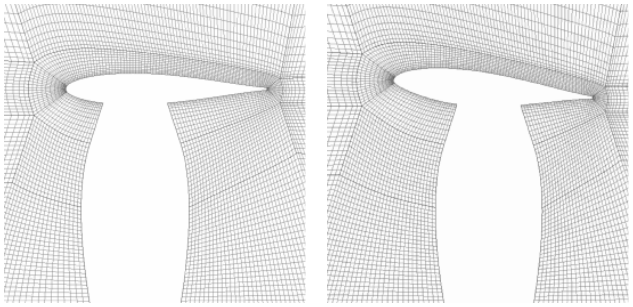

Figure 6: **Surface mesh of the baseline design (left), as well as the optimized geometry variant (right). The images show a part of the rotaionally symmetric static region excluding the nozzle itself, as well as the rotating propeller-region.**

The nozzle region was handled first, by exporting a section of the nozzle, along with the most important components defining the mesh topology. It turned out during this work, that the generation of a structured grid for varying geometry, using the same basic topology, can be challenging in terms of the resulting mesh quality. One major step in improving the grid quality, especially towards criteria like skewness and aspect ratio was, to add the most important parts of the grid topology already within CAESES as a part of the parametric thruster model. This way, they easily adjust to the changing geometry without the need to analyze the shape within the grid generation script and adjust the topology at this stage.

Figure 6 shows the exported geometry of two different nozzles as well as the resulting surface meshes in close proximity to the propeller region. The thickness of the boundary layer region is set, as can bee seen from the dark gray lines surrounding the nozzles. This allows for easy manipulation of the wall spacing and number of layers within the script. To cut the computational costs, as also done during the reference simulations, only a rotational symmetric section was simulated. In this case, as the propeller is two-bladed, the grid needs to cover a 180° region.

Automatic meshing of the propeller region proved to be a lot more complex. Regions like the fillet connecting blade and rim, the sharp trailing edge and the winglet are demanding. Additionally, the blades shape changes over a wide range of parameters which is difficult to handle by one single meshing strategy.

Although different meshing scripts could be applied to certain groups of geometry variants, another reason speaks for a single approach to handle the hole range of parameter combinations. This way, the meshes of two different variants are nearly consistent in topology and the change in between rather equals a mesh morphing than two completely different grids. Especially when comparing geometries that are very similar, the simulation error induced by the quality of the grid could exceed the actual difference in performance of the two variants. However, if the two grids are almost identical, as would also be the case in a traditional mesh morphing approach, the two variants might still be rated from a relative point of view.

To enable the generation of a high quality structured grid for all possible geometry variants, the propeller-region mesh was split into three separate parts arranged as concentric cylinder sections. The cell-faces on the surfaces connecting those regions were again handled by the AMI interpolation functionality within OpenFOAM.

3.3 Objective

As stated within the introductory section, the optimization's objective was to maximize the vessels speed

$$\max \|v_S\| \quad , \tag{10}$$

while using the estimated amount of available power

$$P = P_{est} \quad . \tag{11}$$

However, as the open-water simulations do not include any information on the hull itself, v_S at a given power consumption can not be obtained directly from the CFD results. Instead, an estimation of the self propulsion point (SPP) for each individual design variant under consideration is needed, to quantify v_S.

3.3.1 Estimation of Self Propulsion Point

To estimate the SPP of each design variant, a linear interpolation of K_T and K_Q over a short interval of J was performed. By calculating the power consumption as a function of J, K_T and K_Q, this allows to derive the efficiency of each design variant while propelling the vessel in self propulsion condition at $P = P_{est}$.

The SPP is characterized by the delivered thrust of the thruster matching the resistance of the hull. This dependency can be written as

$$R_T = T\,(1-t) = K_T \rho n^2 D^4\,(1-t) \tag{12}$$

with the thrust deduction coefficient t accounting for the propeller-hull interaction and the correlation $T = K_T \rho n^2 D^4$. The torque coefficient K_T in equation (12) is known from the CFD simulation and the resistance of the hull is determined from experiments in the towing tank at TU Berlin. As no further tests where performed in the tank and also no simulations in any other than open-water status were performed, the thrust deduction coefficient, as well as the wake fraction coefficient were estimated at

$$t = 0.1 \quad \text{and} \quad w = 0.15 \quad .$$

To use the discrete experimental values obtained from the resistance tests as a continuous function of speed in equation (12), a curve-fit based on a least squares approach was done. According to ITTC '57, the total resistance of a ship is described by a frictional resistance coefficient c_F and a number of other coefficients, such as the residual resistance coefficient c_R and additional resistance coefficients accounting for wind, waves and appendages. Hence, the total resistance can be written as:

$$R_T\,(v_S) = c_T \frac{1}{2} \rho v_S^2 S \tag{13}$$

with the total resistance coefficient

$$c_T = c_F + c_R + c_A \quad . \tag{14}$$

The frictional resistance coefficient c_F can be estimated based on the empirical model-ship correlation line fomula in ITTC '57 as:

$$c_F = \frac{0.075}{\left(log_{10}\,(Re) - 2\right)^2} \tag{15}$$

and the above given formulas (13, 14 and 15) can be joined and simplified to

$$R_T\,(v_a) = \frac{a v_a^2}{\left(log_{10}\,(v_a) + b\right)^2} + c v_a^2 \tag{16}$$

$$\text{with} \quad Re = \frac{v_S l}{\nu} \quad \text{and} \quad v_S(1-w) = v_a \quad .$$

The coefficients a, b and c in equation (16) are the parameters determined by the least squares fitting algorithm. They were simply introduced by substituting:

$$a = \frac{0.0375 \rho S}{(1-w)^2} \quad , b = log_{10}\left(\frac{l}{\nu\,(1-w)}\right) - 2 \quad \text{and}$$

$$c = \frac{(c_R + c_A)\,\rho S}{2\,(1-w)^2} \quad .$$

Fitting a curve based on the model function (16) to the experimental data does not necessarily correspond to the determination of any unknown variables in the terms given above. The reason for this is, that these parameters are derived from an empirical formula which is based on a flat plate drag model and additional coefficients that are not a function of the ship speed. However, as the total resistance of the vessel at the speed range under consideration can be assumed to be mainly frictional resistance, the model function was still expected to be applicable for a good approximation of the experimental data.

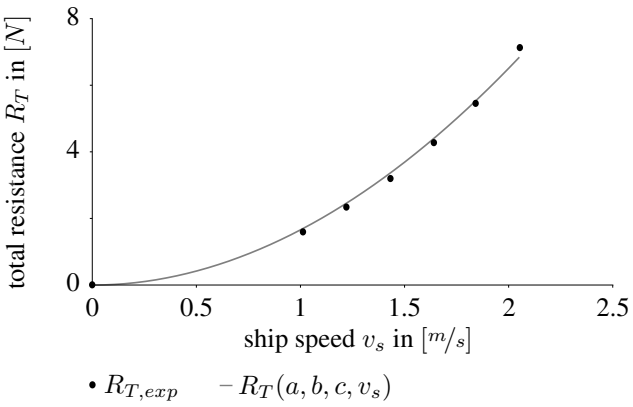

Figure 7: **Discrete experimental findings from the resistance test and the curve fitted based on model function** (16)**.**

The graph in figure 7 shows the curve fitted to the discrete experimental measures based on equation (16). The parameters determined are:

$$a = 42.0456 \quad , b = 8.3354 \quad \text{and} \quad c = 1.0653 \quad .$$

The graph shows a good approximation with a slight overestimation of R_T for all, but the last measure. The sum of squares equals $0.15\ N$ for the given coefficients.

Once the coefficients are known, from the equations (12) and (16) follows:

$$K_T \rho n^2 D^4\,(1-t) = \frac{a v_a^2}{\left(log_{10}\,(v_a) + b\right)^2} + c v_a^2 \quad . \tag{17}$$

Using $v_a = JnD$, the rotational speed can be written as:

$$n\left(J\right) = 10^{\left(\frac{\sqrt{a}JD}{\sqrt{K_T \rho D^4 (1-t) - cJ^2 D^2}} - b - log_{10}(JD)\right)} \quad (18)$$

and the power used by the thuster can be written as a function of J as follows:

$$P\left(J\right) = 2\pi K_Q \rho D^5 n\left(J\right)^3 \quad (19)$$

As stated earlier, the coefficients K_T and K_Q are not known over the hole range of advance coefficients. However, within an interval $[J_1, J_2]$ they can be approximated as a linear function with sufficient accuracy as:

$$K_i\left(J\right) = \frac{K_{i2} - K_{i1}}{J_2 - J_1} J + \left(K_{i2} - \frac{K_{i2} - K_{i1}}{J_2 - J_1} J_2\right) \quad (20)$$

The chosen interval $[J_1, J_2]$ should preferably include the advance ratio in self propulsion condition or at least ensure J_{SPP} lies within close proximity to the bounds.

With the results for both simulations at hand, equation (20) allows for the calculation of the power consumption $P(J)$ according to equation (19). Hence, J_{SPP} can now be determined from the constraint (11). Based on J_{SPP}, now the corresponding values of $K_T(J_{SPP})$ and $K_Q(J_{SPP})$ can be calculated, again using equation (20). With $K_T = K_T(J_{SPP})$, also the rotational speed of the propeller $n(J_{SPP})$ is known and finally, the speed of advance $v_a(J_{SPP})$ and thus, the vessels velocity $v_S(J_{SPP})$ can be calculated based on the definition of the coefficient of advance and the approximation of the wake fraction coefficient. The frictional losses $Q_{rim,end}$ and $Q_{rim,out}$ get added to the torque K_T as a function of the rotational speed n. Consequently, the previously described calculation of the objective measure v_S is an iterative procedure converging towards a rotational speed $n\left(J_{SPP}\right)$ which is the result of calculating the frictional losses based on this exact same rotational velocity $n\left(J_{SPP}\right)$.

As $v_S(J_{SPP}) = v_S(P = P_{est})$, the objective (10) and the constraint (11) of the optimization can be summarized into one single objective:

$$\max \left\| v_S = v_S\left(J_{SPP}, n\left(J_{SPP}, P = P_{est}\right)\right) \right\| \quad . \quad (21)$$

3.4 Exploration Phase

As with most optimization problems, there is no information on the target function within the design space. Therefore, the design space of the optimization is often referred to as a "black box". Inside this black box, the target function may have multiple local minima and maxima. To gain an insight into the approximate behavior of the target function, an exploration algorithm based on a Sobol sequence was used. A total of 25 variants was examined to cover the main influences and interactions between the 5 design variables and build a primary response surface upon the results. The CFD results were post processed automatically and the designs were rated according to their performance in terms of v_S as shown in figure 8. The optimum variant from this phase is hatched for highlighting and served as a starting point for the optimization algorithm.

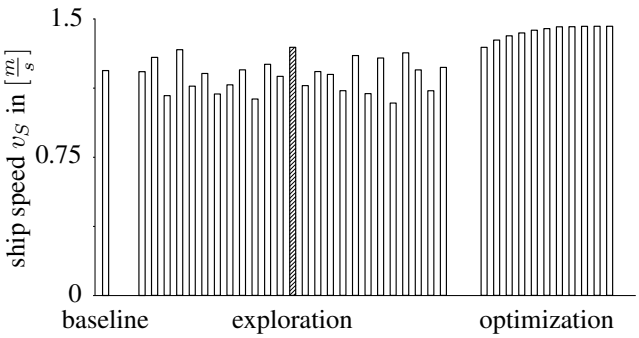

Figure 8: **Comparison of target measure v_S of baseline design ($v_S = 1.22\ ^m/_s$), exploration designs (up to $v_S = 1.34\ ^m/_s$) and optimization phase designs (optimum of $v_S = 1.46\ ^m/_s$).**

3.5 Optimization Phase

The optimization was based on a surrogate model. To enable the use of this kind of algorithm, the external optimization toolbox Dakota was embedded into CAESES. With it comes the possibility of using Response Surface Methodology (RSM) (see Myers 2009) for the optimization task. The response surface allows to estimate the target measure for any point in the design space.

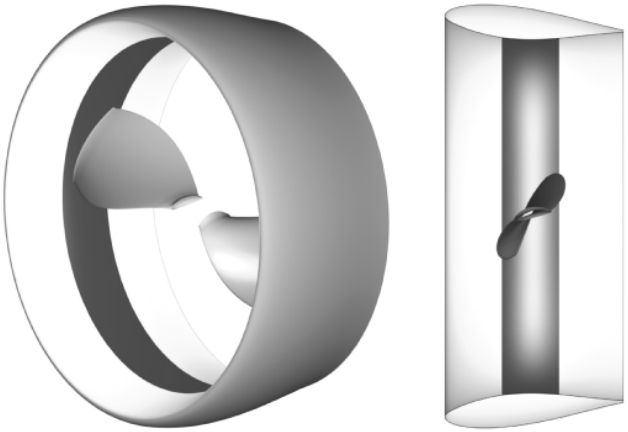

Figure 9: **Optimized RDT design composed of the rotationally symmetric nozzle, propeller ring (shown schematically without the electric motor) and the two blades attached via their tips shown in perspective (left) and section view (right).**

The initial surrogate model was built based on the results of the 25 variants examined during the exploration phase. When using a surrogate model, areas of high potential with respect to the measure of interest need to be resolved with higher precision. Based on the first approximation, the optimum point within the design space was estimated by the surrogate model. As this approximation was based only on those variants examined during the previous exploration

phase, it foreseeable lacked accuracy. Therefore, the determined design point was actually simulated as a next step. The result of the target function was then used to refit the response surface based on all simulations evaluated until this point. This approach increases the accuracy of the surrogate model within the region of interest and allows a better estimate on the optimum variant while the number of iterations increases.

In figure 8, the improvement during the optimization phase is shown. 6 designs are not displayed, as they where rated infeasible due to the violation of $P = P_{est}$. The final thruster design is shown in figure 9 as a complete unit. The corresponding design variables for the nozzle are given in figure 4, the introduced camber is shown in figure 5 and the blade pitch is increased by $4.5\ ^{\circ}$ over the entire radius compared to the baseline variant. As a consequence of the increased P/D ratio, the coefficient of advance at which the optimized variant operates is as high as $J_{SPP} = 1$. As a result, compared to the baseline design, the rotational speed is reduced considerably which again leads to a significant reduction of frictional dissipation within the gap-flow.

As expected, at $T_N = 3.3\ \%$, the amount of thrust generated by the nozzle does not contribute much to the total thrust of the optimized RDT which again is a result of the high coefficient of advance.

4 CONCLUSIONS

Open-water simulations based on OpenFOAM's AMI functionality along with a wall function and k-ω SST turbulence model allow the accurate performance prediction of an RDT as has been shown through reference simulations. CAESES was used to link this setup with an initial fully-parametric model and an automatic grid generation procedure within Pointwise. Frictional dissipation was estimated during post processing and Dakota was embedded into CAESES as an optimization toolbox.

A method of estimating the self propulsion point for a meaningful performance prediction based on CFD results and experimental resistance data of a hull has been presented to allow optimization based on the single objective measure v_S.

During exploration, the calculated ship speeds ranged from $v_S = 1.05\ ^{m}/_{s}$ to $v_S = 1.34\ ^{m}/_{s}$ starting from an initial $v_S = 1.22\ ^{m}/_{s}$ for the baseline design. During optimization a continuous improvement converging towards a final optimum of $v_S = 1.46\ ^{m}/_{s}$ was observed. In terms of open-water efficiency this corresponds to $\eta_o = 0.32$ for the optimized design compared to $\eta_o = 0.19$ for the baseline.

The application of simulation-driven design to the task at hand has proven a very valuable and powerful approach. The results achieved match the expectations and the level of performance predicted is considered satisfactory.

ACKNOWLEDGEMENTS

The authors wish to thank Karsten Rieck from Dynamics of Marine Systems at TU Berlin for conducting the model tests.

Parts of the work presented in this paper were realized within the research and development project HYKOPS, funded by the Federal Ministry of Economics and Technology (BMWi) on the orders of the German Bundestag and PtJ as the conducting agency (FKZ 0303X432).

REFERENCES

Bulten, N. & Suijkerbuijk, R. (2013). 'Full scale thruster performance and load determination based on numerical simulations'. Third International Symposium on Marine Propulsors,

Cao, Q. M., Hong, F. W., Tang, D., Hu, F. & Lu, L. (2011). 'Prediction of loading distribution and hydrodynamic measurements for propeller blades in a rim driven thruster'. Journal of Hydrodynamics, pp. 50-57

Cao, Q. M., Zhao, W. F., Tang, D. & Hong, F. W. (2015). 'Effect of gap flow on the torque for blades in a rim driven thruster without axial pressure gradient'. 7th International Conference on Fluid Mechanics, pp. 680-685

Freeman, M. D. & Marshall, M. A. (2011). 'An analytical investigation into the design of a shaftless thruster using finite element and computational fluid dynamics approaches'. Journal of Ocean Technology, vol. 6, no. 4, pp. 55-68

Grümmer, H., Harries, S. & Cura Hochbaum, A. (2017). 'Optimization of a self-righting hull design and thruster unit for an autonomous surface vehicle'. 16th International Conference on Computer and IT Applications in the Maritime Industries, (to be published), Cardiff, Wales

Hughes, A. W., Turnock, S. R. & Abu Sharkh, S. M. (2000). 'CFD Modelling of a Novel Electromagnetic Tip-Driven Thruster'. School of Engineering Sciences, University of Southampton, Southhampton, USA (unpublished)

Lane, K. A. & Marshall, D. D. (2009). 'A Surface Parameterization Method for Airfoil Optimization and High Lift 2D Geometries Utilizing the CST Methodology'. 47th AIAA Aerospace Sciences Meeting,

Myers, R. H., Montgomery, D. C. & Anderson-Cook, C. M. (2009). Response Surface Methodology. 3rd ed. Wiley (Kindle Edition)

Oosterveld, M. W. C. (1970). 'Wake adapted ducted propellers'. Ph.D. dissertation, Delft University of Technology, Delft, Netherlands

Subhas, S., Saji, V. F., Ramakrishna, S. & Das, H. N. (2012). 'CFD Analysis of a Propeller Flow and Cavitation'. International Journal of Computer Applications, vol. 55

Yakovlev, A. Y., Sokolov, M. A. & Marinich, N. V. (2011). 'Numerical design and experimental verification of a rim-driven thruster'. Second International Symposium on Marine Propulsors

DISCUSSION

Question from Stefano Brizzolara

How did you parameterize the pitch and camber distributions?

Author's closure

Within the parametric model the radial distributions of pitch and camber are both given as B-Spline curves consisting of three points each. In both cases two parameters are used to control the offset of those curves. One allows to add a constant offset over the entire range of radii and another one allows to change the radial distribution by not moving all three points at the same time. However, for the CFD based optimization process only the constant offsets where used as design variables.

Question from Kourosh Koushan

For a hubless propeller, the inner profile does not need to be similar to the root profile of a conventional propeller.

Author's closure

This is correct. The pictures do not show the fillet of a conventional propellers root profile. The increased thickness close to the propeller tip serves the purpose of reducing losses due to tip vortexes. Unlike a fillet it is also not applied near the leading edge as to allow any debris to pass freely through the propeller.